

Annual Review of Physical Chemistry

Capturing Atom-Specific Electronic Structural Dynamics of Transition-Metal Complexes with Ultrafast Soft X-Ray Spectroscopy

Raphael M. Jay,¹ Kristjan Kunnus,² Philippe Wernet,¹ and Kelly J. Gaffney³

¹Department of Physics and Astronomy, Uppsala University, Uppsala, Sweden; email: raphael.jay@physics.uu.se, philippe.wernet@physics.uu.se

²Linac Coherent Light Source, SLAC National Accelerator Laboratory, Menlo Park, California, USA; email: kristjan@slac.stanford.edu

³PULSE Institute, SLAC National Accelerator Laboratory and Stanford University, Menlo Park, California, USA; email: kgaffney@slac.stanford.edu

Annu. Rev. Phys. Chem. 2022. 73:187–208

First published as a Review in Advance on January 5, 2022

The *Annual Review of Physical Chemistry* is online at physchem.annualreviews.org

<https://doi.org/10.1146/annurev-physchem-082820-020236>

Copyright © 2022 by Annual Reviews.
All rights reserved

Keywords

chemical dynamics, electron transfer, photodissociation, X-ray spectroscopy, transition-metal complexes, electronic structure

Abstract

The atomic specificity of X-ray spectroscopies provides a distinct perspective on molecular electronic structure. For *3d* metal coordination and organometallic complexes, the combination of metal- and ligand-specific X-ray spectroscopies directly interrogates metal–ligand covalency—the hybridization of metal and ligand electronic states. Resonant inelastic X-ray scattering (RIXS), the X-ray analog of resonance Raman scattering, provides access to all classes of valence excited states in transition-metal complexes, making it a particularly powerful means of characterizing the valence electronic structure of *3d* metal complexes. Recent advances in X-ray free-electron laser sources have enabled RIXS to be extended to the ultrafast time domain. We review RIXS studies of two archetypical photochemical processes: charge-transfer excitation in ferricyanide and ligand photodissociation in iron pentacarbonyl. These studies demonstrate

ANNUAL
REVIEWS **CONNECT**

www.annualreviews.org

- Download figures
- Navigate cited references
- Keyword search
- Explore related articles
- Share via email or social media

femtosecond-resolution RIXS can directly characterize the time-evolving electronic structure, including the evolution of the metal–ligand covalency.

1. INTRODUCTION

Selectively and efficiently driving chemical transformations remains a persistent and compelling challenge for chemists. From a fundamental perspective, addressing this challenge requires manipulating either the shape of the free energy surface of the reactant to select and accelerate the desired product or how the reactant samples the free energy surface. The first approach can be achieved with a catalyst, the method of choice for the chemical industry and biology. The second approach can be achieved by driving systems far from equilibrium, where nonequilibrium electronic states and geometric structures can be accessed—such as the photoexcitation of a photocatalyst—that also select and accelerate the transformation of reactants to the desired products. For both cases, transition-metal complexes dominate, because they provide extremely flexible and tunable ground- and excited-state electronic structures.

The design and synthesis of molecular catalysts targeting specific reactions have an established history, including five Nobel Prizes in Chemistry awarded to 12 chemists in the twenty-first century for developing molecular catalysts and enzymes (1–11). This research clearly establishes that the appropriate choice of the metal center, the ligands, and their arrangement around the metal center provides a pathway to selective, efficient, and diverse reactions including hydrogenation, epoxidation, cross-coupling, and directed evolution of enzymes. Critical properties of the molecular catalyst include the ligand field strength and symmetry, the oxidation and reduction potentials, the geometric and steric constraints on the inner coordination sphere structure, and the metal–ligand covalency, all of which need to be matched to the metal. Understanding of catalysis by nonequilibrium electronic states and geometric structures remains comparatively rudimentary. The development of photoredox catalysis has been the most significant advance in photon-driven catalysis in the past decade (12–15). Despite this expansion in photocatalysis, a limited number of photocatalysts dominate the research (16, 17), and the design of reaction-specific catalysts, an approach that is characteristic of molecular catalysis, has not yet been matched for photocatalysis.

An analytical characterization gap exists between the number and robustness of the methods used for thermally driven molecular catalysts and those used for characterizing light-driven molecular catalysts. Our review focuses on the electronic structure and reactivity of transition-metal complexes driven far from equilibrium by short light pulses. These pulses have durations in the femtosecond domain. The ultrashort duration of these pulses enables the electronic and geometric structures of light-driven molecules to be changed faster than the reactions initiated by these excited molecules. The ensuing nonequilibrium, photon-driven reaction dynamics is hence triggered and can be followed with a second ultrashort pulse of light synchronized with the trigger pulse. This second pulse interrogates the chemical evolution initiated by the first pulse with an experimentally controlled delay between the pulses. By repeating this measurement and scanning the delay between the first and second pulses, the full-time evolution of the system can be tracked. This method, often termed ultrafast pump-probe spectroscopy, has been used to capture the time-evolution of photochemical reactions from initial femtosecond excited-state dynamics via internal conversion and vibrational cooling on picosecond timescales all the way to diffusion-limited processes on longer timescales. By varying the probe photon energy range from terahertz to hard X-rays and measuring the signal detected from photon absorption, photon elastic and inelastic scattering, and photo-ion or photoelectron production, the information content of the measurement can be modified significantly. Despite the multitude of ultrafast probe methods developed

and used to study light-driven reactivity, it has remained a challenge to disentangle nuclear and electronic dynamics with established ultrafast probes and to achieve the necessary sensitivity to distinguish the many possible chemical intermediates and reaction pathways. Ultrafast X-ray sources producing short X-ray pulses now provide exciting opportunities for probing the electronic and geometric structures of transition-metal complexes.

X-ray free-electron lasers, in particular, provide tunable and highly brilliant X-ray radiation with femtosecond pulse durations enabling measurements of reaction dynamics of very dilute species, as is typical in the chemistry of coordination and organometallic complexes. The progress to date has depended significantly on the wavelength range of the X-rays, in which progress with $<2\text{-}\text{\AA}$ -wavelength hard X-rays has progressed more quickly than with nanometer-wavelength soft X-ray measurements. This work has clearly shown that hard X-ray absorption spectroscopy (18–23), valence-to-core X-ray emission spectroscopy (23, 24), and X-ray solution scattering (25, 26–28) access the geometric structural dynamics surrounding the metal centers in transition-metal complexes. X-ray absorption and emission spectroscopies (23, 25, 29) also access the charge and spin state of the metal center, but they lack the ability to characterize the excited-state electronic structure with state specificity. The development of chemical applications of ultrafast soft X-ray spectroscopy in solution has been slower than the development of hard X-ray spectroscopy due to technical challenges associated with the poorer contrast between solute and solvent absorption, lower fluorescence yields, and the need to work in vacuum (30–44). The purpose of this review is to address the opportunities presented by soft X-ray resonant inelastic X-ray scattering (RIXS) to characterize the electronic structure and dynamics of light-driven transition-metal complexes.

We address this case by discussing time-resolved soft X-ray spectroscopy studies of two archetypical photochemical processes in $3d$ metal coordination and organometallic complexes. We show how probing the valence electronic structure with core-hole spectroscopy provides a compelling and novel approach to interrogating both (*a*) the transient valence electronic structure of charge-transfer excited states in transition-metal coordination complexes and (*b*) the photodissociation dynamics of organometallic metal–carbonyl complexes and the resultant coordination.

The development of ultrafast soft X-ray spectroscopy enables the convergence of three critical capabilities needed to understand how the interplay between electronic and nuclear structures determines the ultrafast dynamics of transition-metal complexes:

1. Ultrafast pump-probe methods enable the controlled generation of electronic excitations and geometric structural evolution. By generating an electronic excitation on the femtosecond timescale, we also generate vibrational wave-packet motion. This motion enables the influence of the nuclear structure on the electronic structure to be followed with precision.
2. Soft X-ray spectroscopy enables electronic states to be interrogated in an atom-by-atom manner that provides unique access to the symmetry and spatial distribution of valence electronic wave functions.
3. Molecular electronic structure theory enables the accuracy of a molecular orbital view of the valence electronic structure to be assessed for ground and electronic excited states.

The combination of these experimental and theoretical capabilities enables the direct determination of how the valence electronic structure evolves during a chemical reaction.

In this review, we describe how core-hole spectroscopies with soft X-rays interrogate the frontier orbitals from both the $3d$ metal and the ligand perspectives, providing a unique ability to experimentally identify the relative importance of the metal and ligand characters of the valence electronic structure. The $2p$ absorption resonances of $3d$ metals ($L_{2,3}$ -edges) and the $1s$ absorption resonances of ligand C, N, and O atoms (K-edges) provide complementary element-specific

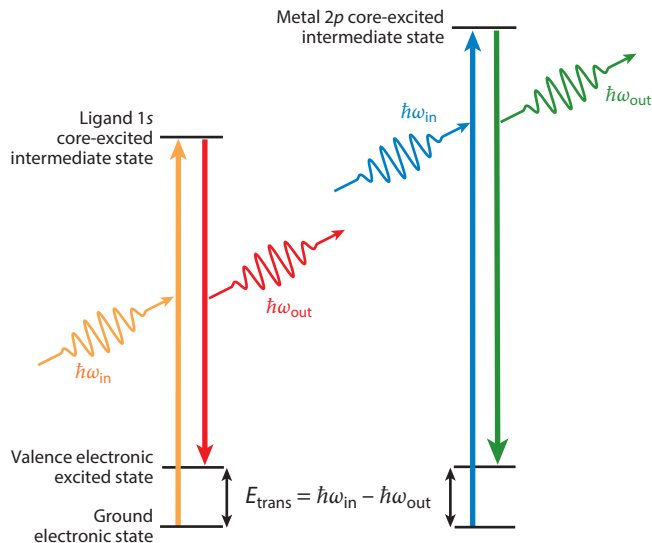


Figure 1

Schematic representation of the spontaneous resonant inelastic X-ray scattering (RIXS) process. Absorption of an incoming X-ray photon, $\hbar\omega_{\text{in}}$, creates a core-excited state intermediate, followed by the emission of a secondary X-ray photon, $\hbar\omega_{\text{out}}$, creating a valence excited final state. The valence electronic excited-state Raman resonances in RIXS spectroscopy, $E_{\text{trans}} = \hbar\omega_{\text{in}} - \hbar\omega_{\text{out}}$, manifest as energy transfer resonances in the eV scale where the resonant energy does not change with the incident X-ray photon energy. RIXS strongly resembles optical resonance Raman scattering, with two critical distinctions. First, the incident X-ray photons ($\hbar\omega_{\text{in}}$) access either the ligand $1s \rightarrow 2p$ or the metal $2p \rightarrow 3d$ core-excited intermediate states rather than a valence excited intermediate state in the visible or ultraviolet light spectrum. Second, RIXS is used to access valence electronic excited final states rather than the vibrationally excited final states accessed with optical resonance Raman scattering.

views of the metal–ligand bonding. Metal $L_{2,3}$ -edge spectroscopy takes the metal perspective and ligand K-edge spectroscopy adopts the ligand perspective, thereby providing an atom-specific measure of the frontier molecular orbitals. This can be achieved for the unoccupied orbitals with X-ray absorption spectroscopy (XAS) (45–47) and for valence excited states with RIXS (48–51), the X-ray analog of resonance Raman scattering (see **Figure 1**). Like spontaneous resonance Raman spectroscopy in the visible and ultraviolet (UV) spectral range, RIXS involves using a light source tuned to an electronic resonance in the system. Unlike optical resonance Raman scattering, the Raman resonances discussed in our review focus on valence electronic excitations rather than the vibrational excitations that dominate optical resonance Raman spectroscopy.

RIXS relies on strong electric dipole transitions with metal $2p \rightarrow 3d$ and ligand $1s \rightarrow 2p$ excitations, making the methods sensitive to small changes in the electronic structure. Chemical shifts of the respective core-electron resonances make the methods sensitive to changes at specific chemical sites, including atoms of the same element in different chemical environments (52). This enables XAS and RIXS to characterize frontier molecular orbitals with element and site specificity (23). Compared to UV and visible absorption spectroscopy and other more established probes of molecular electronic structure, we highlight how the large energy scale probed with X-ray spectroscopy and the selection rules of the measurement ensure sensitivity to all classes of electronic excited states irrespective of metal or ligand nature and the spin state.

This sets the stage for discussing the incipient results acquired with ultrafast soft X-ray spectroscopy studies of the photophysical and photochemical dynamics of prototypical

transition-metal compounds in solution. We close by providing an outlook on the quickly evolving capabilities of X-ray free-electron laser sources, instrumentation, and how this should transform chemical dynamics applications.

2. ELECTRONIC STRUCTURE AND DYNAMICS OF TRANSITION-METAL COMPLEXES

2.1. Introduction to Soft X-Ray Resonant Inelastic X-Ray Scattering

Metal–ligand bonding is rationalized by a hybridization of the partially occupied metal *d* orbitals with occupied and unoccupied ligand orbitals, thereby creating new bonding and antibonding combinations of molecular orbitals (see **Figure 2a**). The ligand field reduces the symmetry of the free metal atom and lifts the degeneracy of the metal *d* orbitals in a manner dictated by the

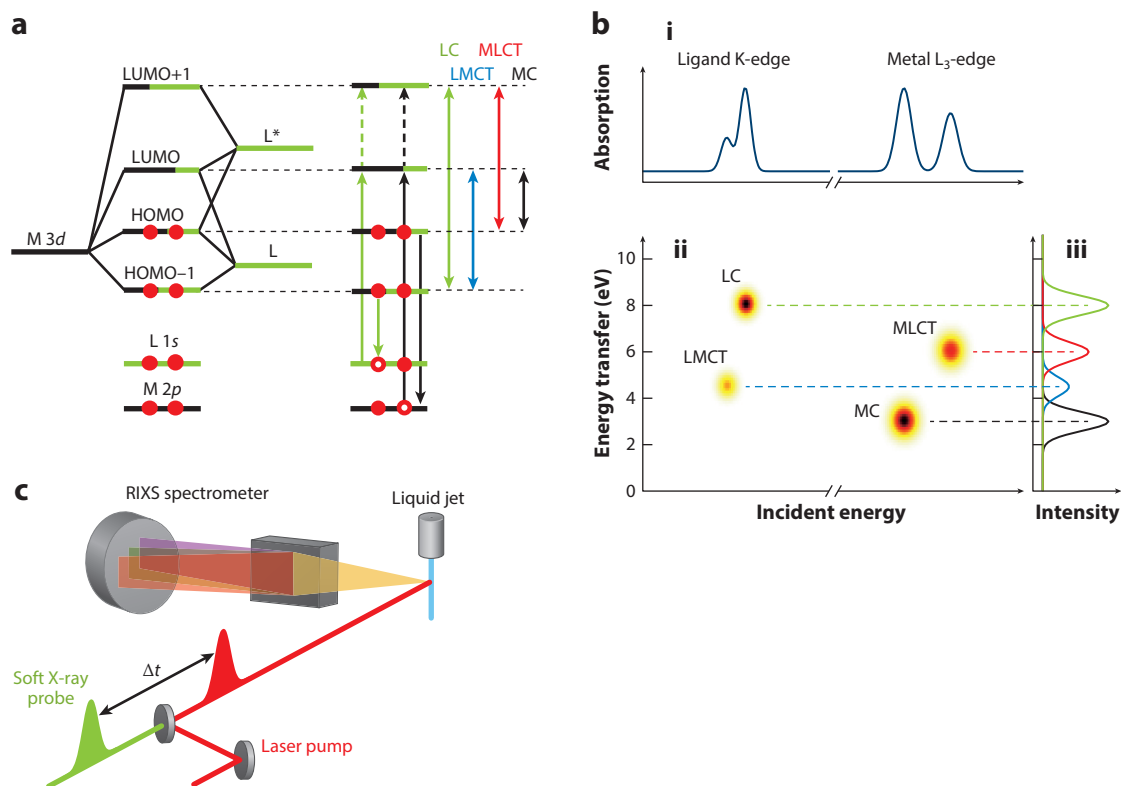


Figure 2

(a) Schematic representation of the hybridization between metal and ligand orbitals underlying the metal–ligand bonding in transition-metal complexes. Distinct from the most general, state-specific depiction of RIXS shown in **Figure 1**, the right side of this panel shows how RIXS uses atom-specific absorption resonances to access specific orbitals and yield specific valence excited final states.

(b) Exemplary (i) X-ray absorption spectroscopy spectra and (ii) RIXS maps and (iii) spectra as typically acquired at metal L₃- and ligand K-edges. The respective amplitudes of the core-excited intermediate and valence excited final states can be directly related to the atomic character of the involved orbitals. (c) Schematic representation of the typical experimental scheme of time-resolved RIXS experiments. The solution sample is optically excited by a laser pulse and probed by a soft X-ray pulse at a specific time delay. The resulting inelastically scattered light is detected with an emission spectrometer as a function of incident X-ray energy and pump-probe time delay (Δt). Abbreviations: HOMO, highest-occupied molecular orbital; L, ligand; LC, ligand centric; LMCT, ligand-to-metal charge transfer; LUMO, lowest-unoccupied molecular orbital; M, metal; MC, metal centric; MLCT, metal-to-ligand charge transfer; RIXS, resonant inelastic X-ray scattering.

coordination shell structure. For the majority of transition-metal complexes, the highest-occupied molecular orbital (HOMO) and the lowest-unoccupied molecular orbital (LUMO) have predominantly metal character, as indicated in **Figure 2a**. The frontier d orbital energies of the free metal atom split according to the symmetry of the ligand field. Depending on the exact ligand and coordination structures, the hybridized metal d orbitals can acquire partial ligand character. While this interaction gives the metal d orbitals some amplitude on the ligand, in an LCAO (linear combination of atomic orbitals) approach, they are referred to as metal-derived orbitals. In turn, the bonding and antibonding hybridized ligand orbitals also acquire metal character. This creates new occupied and unoccupied molecular orbitals of the complex; see the HOMO-1 and LUMO+1 in **Figure 2a**, which have a degree of metal character but can still be classified as ligand character-derived orbitals.

The ability to project the complex electronic structures of molecules onto their atomic constituents presents one of the most compelling conceptual strengths of X-ray spectroscopies. Connecting experimental spectroscopic observables to this conceptual framework relies on multiple approximations. Within the constraints of these approximations, a qualitative and intuitive description of the covalent electronic structure of transition-metal complexes can be achieved. Here we discuss how an atomic decomposition of the molecular orbitals can be extracted from RIXS measurements.

RIXS measures the inelastically scattered X-rays spontaneously emitted from a sample when excited with X-rays tuned to an absorption resonance (**Figure 1**). The cross section for RIXS can be calculated with the Kramers-Heisenberg formula (53, 54),

$$I_{\text{RIXS}} \propto \frac{|\langle f | \mu | i \rangle \langle i | \mu | g \rangle|^2}{(E_g - E_i + \hbar\omega_{\text{in}} + i\frac{\Gamma_i}{2})} \delta(E_i - E_f + \hbar\omega_{\text{in}} - \hbar\omega_{\text{out}}),$$

where $\hbar\omega_{\text{in}}$ and $\hbar\omega_{\text{out}}$ are the energies of the incident and inelastically scattered X-ray photons; $|g\rangle$ is the ground, $|i\rangle$ the intermediate, and $|f\rangle$ the final electronic states involved in the RIXS process; E_g , E_i , and E_f are the energies of the ground, intermediate, and final electronic states; Γ_i is the lifetime broadening of the intermediate state; and μ is the transition dipole moment operator that couples X-rays to the electrons in the sample. For RIXS, the incident photon energy $\hbar\omega_{\text{in}}$ equals the energy gap between the ground and intermediate electronic states, $E_A = E_i - E_g$, corresponding to an absorption resonance. Additionally, the energy difference between the incident and scattering photon, $E_{\text{trans}} = \hbar\omega_{\text{in}} - \hbar\omega_{\text{out}}$, equals the energy difference between the intermediate and final state energies, $E_{\text{trans}} = E_i - E_f$, corresponding to a Raman energy transfer resonance.

A minimalist and simplified view of the electronic structure of transition-metal complexes illustrates how the RIXS spectrum accesses the covalent hybridization of metal and ligand orbitals. Consider a metal complex composed of a transition metal and an atomic ligand. The complex has a HOMO, ψ_{HOMO} , and a LUMO, ψ_{LUMO} , with mixed metal-ligand character due to the covalent hybridization of the metal and ligand valence orbitals. Within an LCAO description of the valence molecular orbitals, we have

$$\begin{aligned}\psi_{\text{HOMO}} &= \alpha_M 3d_M + \alpha_L 2p_L, \\ \psi_{\text{LUMO}} &= \beta_M 3d_M + \beta_L 2p_L.\end{aligned}$$

The RIXS process accesses the covalency via the magnitude of the matrix elements in the numerator in the Kramers-Heisenberg formula above. For the sake of conceptual clarity, we approximate the ground $|g\rangle$, intermediate $|i\rangle$, and final $|f\rangle$ states included in these matrix elements by

including only active orbitals involved in the inelastic scattering, and we consider ligand K-edge or 1s RIXS as an example. Specifically,

$$\begin{aligned}|g\rangle &= |1s_L^2 \psi_{\text{HOMO}}^2 \psi_{\text{LUMO}}\rangle, \\ |i\rangle &= |1s_L^1 \psi_{\text{HOMO}}^2 \psi_{\text{LUMO}}^1\rangle, \\ |f\rangle &= |1s_L^2 \psi_{\text{HOMO}}^1 \psi_{\text{LUMO}}^1\rangle,\end{aligned}$$

where the superscript presents the number of electrons in the orbital. The RIXS matrix elements for a ligand core-hole resonance can be simplified as

$$| \langle 1s_L^2 \psi_{\text{HOMO}}^1 \psi_{\text{LUMO}}^1 | \mu | 1s_L^1 \psi_{\text{HOMO}}^2 \psi_{\text{LUMO}}^1 \rangle \langle 1s_L^1 \psi_{\text{HOMO}}^2 \psi_{\text{LUMO}}^1 | \mu | 1s_L^2 \psi_{\text{HOMO}}^2 \psi_{\text{LUMO}} \rangle |^2.$$

The strong localization of the $|1s_L\rangle$ orbital in space at the location of the ligand nuclei ensures that the transition dipole moment operator only couples the $|1s_L\rangle$ orbital to valence orbitals with spatial density at the ligand nuclei with appropriate symmetry. Consequently, the strength of this RIXS signal reflects the covalent mixing of the occupied and unoccupied orbitals involved in the RIXS transition. Highlighting only the ligand atomic components of the orbitals involved gives a RIXS spectrum proportional to

$$I_L^{\text{RIXS}} \propto \alpha_L^2 \beta_L^2 | \langle 1s_L | \mu | 2p_L \rangle \langle 2p_L | \mu | 1s_L \rangle |^2.$$

Analogously, at a metal resonance, the RIXS signal strength is proportional to

$$I_M^{\text{RIXS}} \propto \alpha_M^2 \beta_M^2 | \langle 2p_M | \mu | 3d_M \rangle \langle 3d_M | \mu | 2p_M \rangle |^2.$$

Our review now focuses on how this conceptual framework manifests in an experimental RIXS spectrum for ground and optically generated valence electronic excited states.

Figure 2a provides a schematic description of the electronic structure of a transition-metal complex, and **Figure 2b** shows how this electronic structure manifests itself in the RIXS spectrum by focusing on four selected RIXS transitions that typically dominate the RIXS intensities at ligand K-edges and 3d metal L-edges. In a RIXS experiment, the incident X-ray photon energy is scanned through the element-specific ligand K-edge or metal L-edge resonances, and the energy of the inelastically scattered photons is measured to determine the energy transferred to the system as a function of incident photon energy. The energy transfer can correspond to vibrational (55, 56) or electronic excitations in the sample, and here we focus on electronic excitations.

As described above, the resonant interaction of the incident X-rays creates an intermediate state in which the ligand (L, **Figure 2**) 1s or metal (M, **Figure 2**) 2p core electron is promoted to an unoccupied molecular orbital (LUMO or LUMO+1 in **Figure 2**). Overall, the final states of the RIXS process as described here are valence excited states involving metal-centric (MC) and ligand-centric (LC) excitations or excitations that involve electron transfer between the metal and ligand [metal-to-ligand charge transfer (MLCT) and ligand-to-metal charge transfer (LMCT)]. The character of these final states is determined by the orbitals involved in the RIXS transitions. In the exemplary case described in **Figure 2**, the core excitations at the ligand K-edge involve the metal-derived LUMO or the ligand-derived LUMO+1 and the HOMO–1 orbital. RIXS at the ligand K-edge therefore probes LMCT or LC excited states. RIXS at the metal L-edge, besides addressing the same LUMO and LUMO+1 orbitals, also involves the metal-derived HOMO orbital and hence results in MC and MLCT excited states (**Figure 2b**). In combination, ligand K-edge and metal L-edge RIXS therefore give access to the full range of valence excited final states of transition-metal complexes, which can be disentangled by tuning the incident energy. Note that the coherence between the incident and emitted photons does not affect the interpretation of the

RIXS spectra presented in this review. The role of coherence in RIXS has been reviewed previously (53, 54).

Figure 2c depicts a schematic representation of the optical pump soft X-ray probe RIXS experiment, which we discuss briefly. A short-duration optical pulse excites the sample, and a short-duration monochromatic soft X-ray probe pulse interrogates the pump-induced dynamics by collecting a RIXS spectrum of scattered probe photons. An energy resolution of 0.3 to 1.0 eV is required to record RIXS spectra with chemical sensitivity. Although conceptually simple, experimental realization of such measurements has a number of challenges worthy of emphasis. Most importantly, RIXS requires tunable monochromatic pulses of sub-100-femtosecond duration with high flux. The need for high flux is dictated by two factors: (a) the intrinsically low cross section of the RIXS process in the soft X-ray range and (b) the technical difficulties associated with collecting soft X-rays with a spectrometer. The low cross section results from the dominance of Auger decay in the soft X-ray range with which the core-excited intermediate states decay. Consequently, the yield of fluorescent decay, in which the core hole is filled via the emission of a secondary photon, is typically <1%. For example, the yield of N $2p \rightarrow 1s$ radiative decay is 0.53% and the Fe $3d \rightarrow 2p$ fluorescence yield is 0.63% (57). The main difficulty in collecting and dispersing soft X-ray radiation is associated with the low efficiency of soft X-ray spectrometers. This is primarily due to the small geometric acceptance of the grazing-angle ($\sim 1^\circ$) optics, which are needed to have appreciable reflectivity of soft X-rays. Typical efficiencies of soft X-ray spectrometers are on the order of 1×10^{-6} , assuming isotropic emission of fluorescence/RIXS photons from the sample. In addition, soft X-ray spectrometers require a small source size ($\sim 20\text{-}\mu\text{m}$ area from which the inelastically scattered light can be accepted) in order to have sufficient resolution given the limited grating dispersion in the soft X-ray wavelength range and detector pixel size. Currently, only large-scale X-ray free-electron laser facilities can deliver photons suitable for pump-probe RIXS experiments. For high peak intensity X-ray sources, the liquid must be injected into vacuum in the form of a jet (58–60).

2.2. Electronic Structure of Charge-Transfer Excited States in Ferricyanide

Ferric and ferrous hexacyanide have been critical to the development of ligand field theory (61, 62) as well as molecular spectroscopy (63–66), and therefore provide natural complexes for the development of ultrafast RIXS to characterize the electronic structure of transition-metal complexes in electronic excited states. **Figure 3a** shows the molecular structure and orbital diagram of ferric hexacyanide, $[\text{Fe}^{\text{III}}(\text{CN})_6]^{3-}$. $[\text{Fe}^{\text{III}}(\text{CN})_6]^{3-}$ is a doublet $3d^5$ low-spin complex with the $3d$ levels split by the octahedral ligand field into the occupied t_{2g} and unoccupied e_g levels. As strong σ -donating ligands, the e_g symmetry-adapted combination of CN^- σ and Fe $3d$ orbitals forms bonding orbitals dominated by $\text{L}\sigma$ molecular orbitals as well as an antibonding combination of CN^- and Fe $3d$ molecular orbitals dominated by Fe $3d(e_g)$ molecular orbitals. At the same time, the $3d(t_{2g})$ orbitals possess $\text{L}\pi^*$ character via a π -back donation interaction, and the unoccupied $\text{L}\pi^*$ orbitals also possess $3d(t_{2g})$ character. These orbital interactions make up the metal–ligand bond. How these interactions can be uniquely assessed using XAS and RIXS in the soft X-ray regime was studied in detail before (50, 67, 68) and is summarized below.

Figure 3d,e shows the RIXS maps of $[\text{Fe}^{\text{III}}(\text{CN})_6]^{3-}$ measured at the N K- and Fe L_3 -edges (50). Plotting the integrated intensity of the scattered photons as a function of incident photon energy generates the partial fluorescence yield (PFY) XAS spectra shown in **Figure 3b,c**. At the N K-edge (**Figure 3b**), the PFY XAS and RIXS spectra are dominated by a strong absorption at 399.6 eV. This peak can be assigned to the N $1s \rightarrow \text{L}\pi^*$ transition associated with the strong N $2p$ character of the CN^- π^* system. At the lower incidence energy of 398.5 eV, a shoulder corresponding to an N $1s \rightarrow 3d(e_g)$ transition can be observed. The nonzero amplitude of this

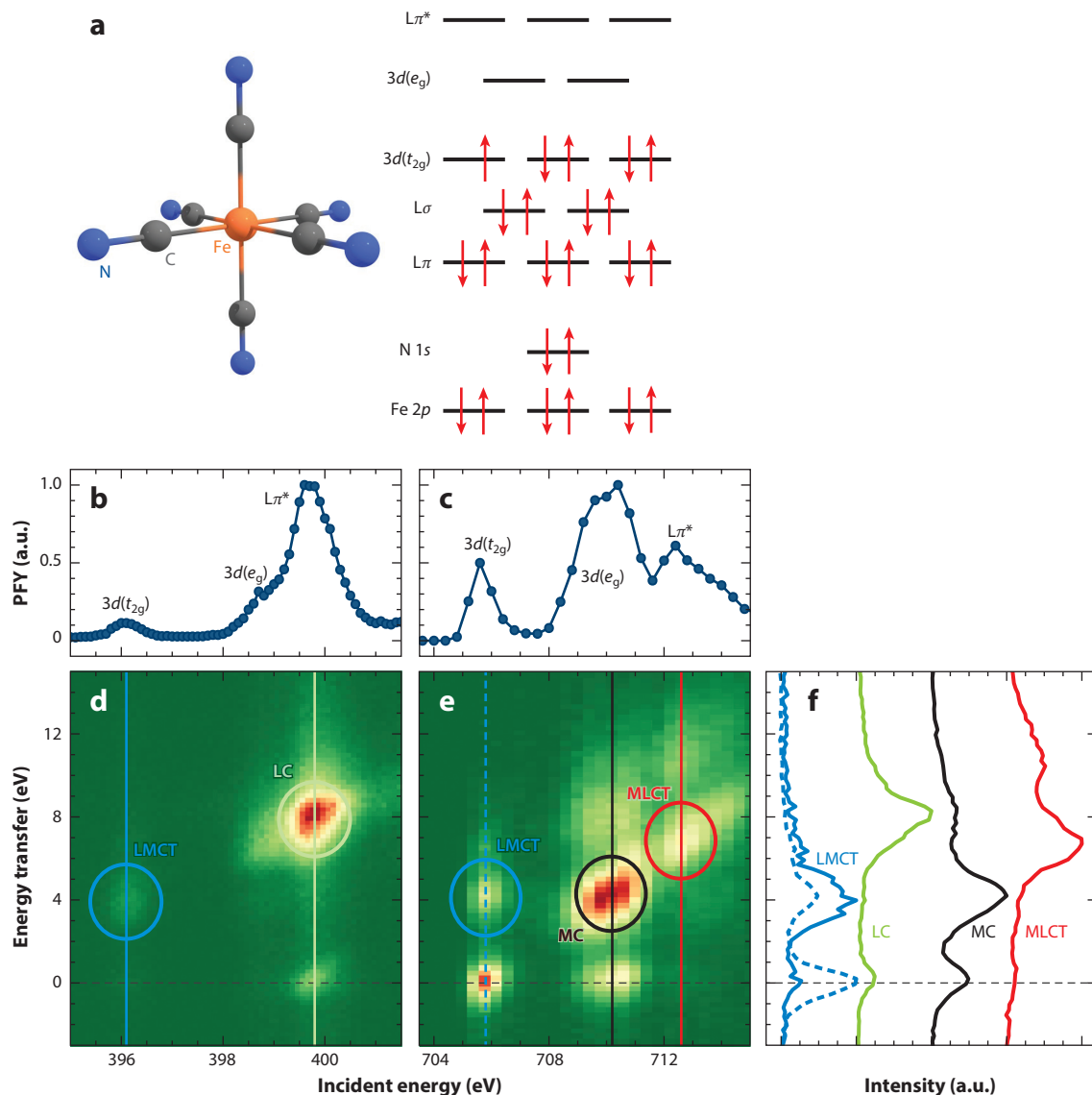


Figure 3

(a) Molecular structure and orbital diagram of $[\text{Fe}^{\text{III}}(\text{CN})_6]^{3-}$. (b,c) PFY X-ray absorption spectrum and (d,e) RIXS map of $[\text{Fe}^{\text{III}}(\text{CN})_6]^{3-}$ measured at the N K-edge and Fe L₃-edge, respectively. The dominant core-excited intermediate states in the PFY spectrum are labeled consistent with the molecular orbitals in panel a. The valence excited final states in the RIXS maps are labeled according to their final state character. The e_g symmetry-adapted combination of CN^- σ and Fe $3d$ orbitals forms bonding orbitals dominated by $L\sigma$ molecular orbitals as well as an antibonding combination of CN^- and Fe $3d$ molecular orbitals dominated by Fe $3d(e_g)$ molecular orbitals. At the same time, the $3d(t_{2g})$ orbitals possess $L\pi^*$ character via a π -back donation interaction, and the unoccupied $L\pi^*$ orbitals also possess $3d(t_{2g})$ character. (f) RIXS spectra for selected incident photon energies. The line colors and styles of the spectra in f match the concomitant vertical lines in the RIXS maps in panels d and e. Abbreviations: L, ligand; LC, ligand centric; LMCT, ligand-to-metal charge transfer; MC, metal centric; MLCT, metal-to-ligand charge transfer; PFY, partial fluorescence yield; RIXS, resonant inelastic X-ray scattering. Adapted with permission from Reference 50; copyright 2016 the American Chemical Society.

transition reflects the N $2p$ contributions to the $3d(e_g)$ orbital resulting from the metal–ligand σ bonding. Lastly, the transition peak at 396.1 eV results from an N $1s \rightarrow 3d(t_{2g})$ transition. The minor amplitude of this peak reflects the comparably smaller N $2p$ character present in the $3d(t_{2g})$ orbitals resulting from π back donation.

Transitions of analogous character also appear at the Fe L_3 -edge (**Figure 3b**). The two features at 705.6 eV and 710.0 eV correspond to Fe $2p \rightarrow 3d(t_{2g})$ and Fe $2p \rightarrow 3d(e_g)$ transitions. Due to the metal-centered character of the $3d(t_{2g})$ and $3d(e_g)$ orbitals, these transitions gain significantly in amplitude compared to transitions to ligand-centered orbitals. In contrast to the analogous transition at the N K-edge involving the same $3d(t_{2g})$ and $3d(e_g)$ orbitals, they dominate the Fe L-edge spectrum. The additional absorption feature on the high-energy side of the spectrum at 712.5 eV corresponds to Fe $2p \rightarrow L\pi^*$ transitions. This transition to a ligand-dominated orbital with π symmetry becomes possible due to the orbital mixing resulting from π back donation from the Fe atom, which adds Fe $3d$ contributions to the $L\pi^*$ orbital. Note that the amplitude of this feature provides a measure of the π back bonding, information that is hard to access with other methods (67, 69, 70). The strong intensity of this feature in the Fe L-edge PFY XAS spectrum, however, cannot be solely understood within the qualitative electronic structure description used here (67). Quantitative interpretations of the spectrum, in terms of accurate descriptions of both intensities and energies, require more sophisticated theoretical descriptions of the electronic structure (48, 50, 68, 71, 72).

Measuring the intensities of inelastically scattered photons as a function of incident X-ray energy generates the RIXS maps shown in **Figure 3d** and **e**, in which the energy transfer is the difference between incident and scattered X-ray photon energy. This energy transfer directly corresponds to the energy of the valence excited final states generated by RIXS. Plotting RIXS intensities at selected incident energies enables specific final states and their energies to be associated with specific intermediate excited states. This proves critical to the interpretation of the spectra shown in **Figure 3f**. Importantly, RIXS enables the same final states to be accessed from both ligand and metal core resonances, as shown in **Figure 3d–f**. Specifically, the N K-edge and the Fe L_3 -edge RIXS spectra access the same LMCT final state with the same energy transfers, albeit with mutually exchanged intensities. The peak at an energy transfer of 4 eV corresponds to an LMCT ($L\sigma \rightarrow t_{2g}$) final state configuration (with the orbital energy diagram in **Figure 3a**, the overall inelastic scattering process can be regarded as N $1s \rightarrow 3d(t_{2g})$ and Fe $2p \rightarrow 3d(t_{2g})$ transitions followed by $L\sigma \rightarrow N 1s$ and $L\sigma \rightarrow Fe 2p$ transitions). The mutually exchanged peak intensities for the LMCT final state in **Figure 3f** directly reflect the different degrees of overlap of the $L\sigma$ orbital with the N $1s$ or Fe $2p$ core holes. The $L\sigma$ orbital, having stronger ligand than metal character, has a larger overlap with the N $1s$ core hole, which in turn makes $L\sigma \rightarrow N 1s$ transitions stronger than $L\sigma \rightarrow Fe 3d$ transitions; this is expressed in the higher intensity of the 4 eV RIXS peak as extracted at the N K-edge.

The most intense peak in the N K-edge RIXS map has an incident energy of 399.6 eV and an energy transfer of 8 eV. The strong intensity reflects the significant overlap between the N $1s$ core hole and the $L\pi$ and $L\pi^*$ orbitals involved in the corresponding RIXS scattering. The correspondingly strong peak in the RIXS spectrum (**Figure 3f**) can therefore be attributed to LC valence excited states resulting from $L\pi \rightarrow L\pi^*$ transitions. Analogously, the most intense peak in the Fe L_3 -edge RIXS map at an incident energy of 710.0 eV and an energy transfer of 4 eV (**Figure 3f**) is intense due to the strong Fe character of the $3d(t_{2g})$ and $3d(e_g)$ orbitals. It can be assigned to an MC final state involving $3d(t_{2g}) \rightarrow 3d(e_g)$ transitions [Fe $2p \rightarrow 3d(e_g)$ followed by $3d(t_{2g}) \rightarrow Fe 2p$] and constitutes a direct measure of the ligand field splitting. This is one example of how the RIXS process preferentially accesses valence excited states that cannot be accessed with absorption spectroscopy in the UV and visible spectrum, because the strong,

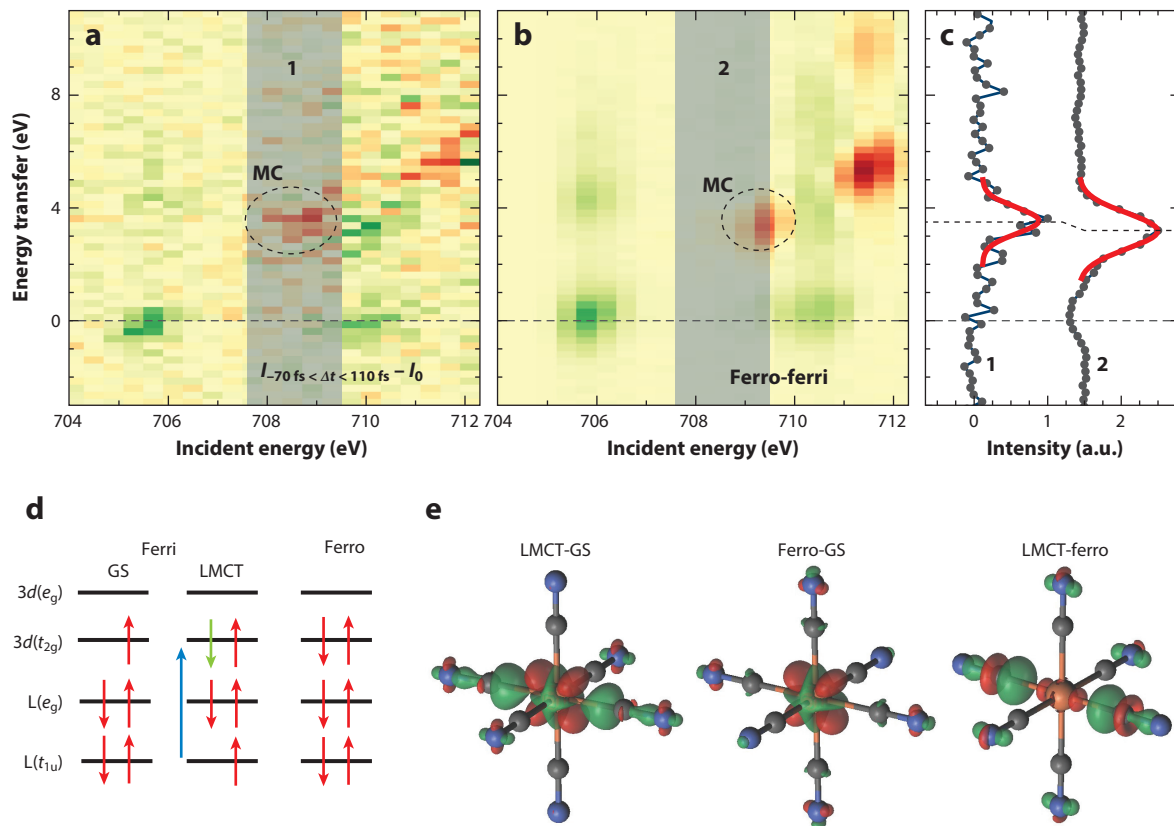


Figure 4

Difference RIXS maps between (a) the LMCT and GS of $[\text{Fe}^{\text{III}}(\text{CN})_6]^{3-}$ and (b) the GSs of $[\text{Fe}^{\text{II}}(\text{CN})_6]^{4-}$ and $[\text{Fe}^{\text{III}}(\text{CN})_6]^{3-}$. (c) RIXS spectra extracted by integrating along the marked incident energy regions in panels a and b, revealing a shift in energy transfer for the MC [$3d(t_{2g}) \rightarrow 3d(e_g)$] valence excited final state as determined by a Gaussian fit (red lines). (d) Orbital occupation in the LMCT and GS of $[\text{Fe}^{\text{III}}(\text{CN})_6]^{3-}$ as well as $[\text{Fe}^{\text{II}}(\text{CN})_6]^{4-}$ (blue arrow represents the ligand-to-metal charge-transfer excitation by the pump pulse). (e) Calculated charge-density differences between the LMCT and GSs of $[\text{Fe}^{\text{III}}(\text{CN})_6]^{3-}$, the GSs of $[\text{Fe}^{\text{II}}(\text{CN})_6]^{4-}$ and $[\text{Fe}^{\text{III}}(\text{CN})_6]^{3-}$ as well as the LMCT state of $[\text{Fe}^{\text{III}}(\text{CN})_6]^{3-}$, and the GS of $[\text{Fe}^{\text{II}}(\text{CN})_6]^{4-}$, where red indicates a charge-density increase and green a decrease. Abbreviations: Ferri, ferric hexacyanide; Ferro, ferrous hexacyanide; GS, ground state; L, ligand; LMCT, ligand-to-metal charge transfer; MC, metal centric; RIXS, resonant inelastic X-ray scattering. Figure adapted with permission from Reference 35; copyright 2018 the American Chemical Society.

optically allowed charge-transfer and ligand-centered excitations obscure the Laporte forbidden ($\Delta L \neq \pm 1$) metal-centered valence excitations.

Extending the demonstrated capability of RIXS to probe the metal–ligand covalency of the electronic ground state to electronic excited states motivated our investigation of the LMCT excitation in $[\text{Fe}^{\text{III}}(\text{CN})_6]^{3-}$ (73–75) with femtosecond time-resolved RIXS (35). A 400-nm laser excitation elevates an electron from a ligand orbital of t_{1u} symmetry and predominant π character into the t_{2g} hole of predominantly metal $3d$ -orbital character (**Figure 4**) (61). To first order, this electronic excited state adopts a d^6 configuration comparable to ferrous hexacyanide $[\text{Fe}^{\text{II}}(\text{CN})_6]^{4-}$. The RIXS spectral response to the LMCT excitation is shown as a RIXS difference map in **Figure 4a**.

Figure 4b shows the difference RIXS spectra for the electronic ground states of $[\text{Fe}^{\text{II}}(\text{CN})_6]^{4-}$ and $[\text{Fe}^{\text{III}}(\text{CN})_6]^{3-}$ (50). When comparing the difference map generated from these ground-state

spectra to that generated by the LMCT excitation of $[\text{Fe}^{\text{III}}(\text{CN})_6]^{3-}$, the similarities are striking. In particular, RIXS final states at the $2p \rightarrow 3d(t_{2g})$ resonance at 705.6 eV incident energy exhibit significant bleach in both cases. This directly reflects how the LMCT excitation fills the single hole in the t_{2g} orbital, generating an electronic configuration analogous to that of $[\text{Fe}^{\text{II}}(\text{CN})_6]^{4-}$ (compare **Figure 4d**). This similarity is also supported by the charge density extracted from quantum chemical calculations (76, 77) shown in **Figure 4e**. Locally, at the metal, the charge-density differences between the LMCT and the ground state of $[\text{Fe}^{\text{III}}(\text{CN})_6]^{3-}$ exhibit a qualitative behavior similar to the difference between the ground states of $[\text{Fe}^{\text{II}}(\text{CN})_6]^{4-}$ and $[\text{Fe}^{\text{III}}(\text{CN})_6]^{3-}$. This can be seen by the uniform increase in charge density at the metal in the shape of a $3d(t_{2g})$ orbital in both charge-density differences (**Figure 4e**). In both cases, however, an additional decrease in σ -like charge density locally at the metal can be observed. This is due to an increase in Coulomb repulsion between the metal and ligand electrons caused by the higher occupation of metal-derived orbitals in $[\text{Fe}^{\text{II}}(\text{CN})_6]^{4-}$ as well as the LMCT state, which subsequently lowers the amount of charge density being delocalized onto the metal via σ donation.

While this behavior is qualitatively the same for the LMCT excitation and $[\text{Fe}^{\text{II}}(\text{CN})_6]^{4-}$, the two cases differ quantitatively in terms of the decrease in σ donation. Whereas the electronic structure calculations suggest σ donation decreases by 25% for the LMCT excitation, it decreases by 39% for the ferrous complex. This demonstrates the effect the ligand hole has on the valence electronic structure, which is also reflected in the experiment. In both RIXS difference maps, the intensities at an incident energy of 709 eV and energy transfer from 3 to 3.5 eV can be assigned to MC final states involving $3d(t_{2g}) \rightarrow 3d(e_g)$ transitions (50, 71). The energy transfer of these features therefore directly reflects the ligand field splitting in the two different electronic configurations. The corresponding RIXS spectra displayed in **Figure 4c** show that the ligand field splitting is larger in the LMCT state by 0.3 eV than in $[\text{Fe}^{\text{II}}(\text{CN})_6]^{4-}$. This is a consequence of the aforementioned higher σ donation in the case of the LMCT state, as an increase in σ donation destabilizes the metal–ligand antibonding $3d(e_g)$ orbitals and thus increases the ligand field splitting.

The reason for the higher σ donation in the LMCT state is the character of the ligand hole. As can be seen in the charge-density difference between the LMCT and ground state of $[\text{Fe}^{\text{III}}(\text{CN})_6]^{3-}$ (**Figure 4e**), the decrease in charge density on the ligand representing the hole has significant σ character. This effectively creates a charge vacancy with σ character, which favors an increase in σ donation. This in turn also corresponds to a higher delocalization of ligand electronic charge onto the metal caused by the hole on the ligand in the LMCT state. When directly comparing the charge-density difference between the LMCT state of $[\text{Fe}^{\text{III}}(\text{CN})_6]^{3-}$ and that of the ground state of $[\text{Fe}^{\text{II}}(\text{CN})_6]^{4-}$ (see **Figure 4e**), this manifests as an increase in charge at the metal in the LMCT state. Experimentally, this can also be seen from the incident energy of the Fe $2p \rightarrow 3d(e_g)$ absorption transition, which has a lower incident energy for the case of the LMCT state than does $[\text{Fe}^{\text{II}}(\text{CN})_6]^{4-}$. The position of this absorption onset and therefore the incident energy necessary for a core excitation can be related to the composition of the local charge distribution around the metal and how efficiently it can screen the core hole in the core-excited intermediate state (a higher local charge reduces the energy of the core excitation) (70, 78). The shift of the absorption onset between the LMCT state and $[\text{Fe}^{\text{II}}(\text{CN})_6]^{4-}$ provides an experimental signature of the predicted increase in electronic charge locally at the metal in the LMCT state as a result of the higher σ donation than in $[\text{Fe}^{\text{II}}(\text{CN})_6]^{4-}$.

2.3. Electronic Structure and Dynamics Induced by Photodissociation of Iron Pentacarbonyl

Metal–carbonyl bond photodissociation has proven to be a powerful photochemical platform for advancing our mechanistic understanding of bond activation and catalysis, as well as developing

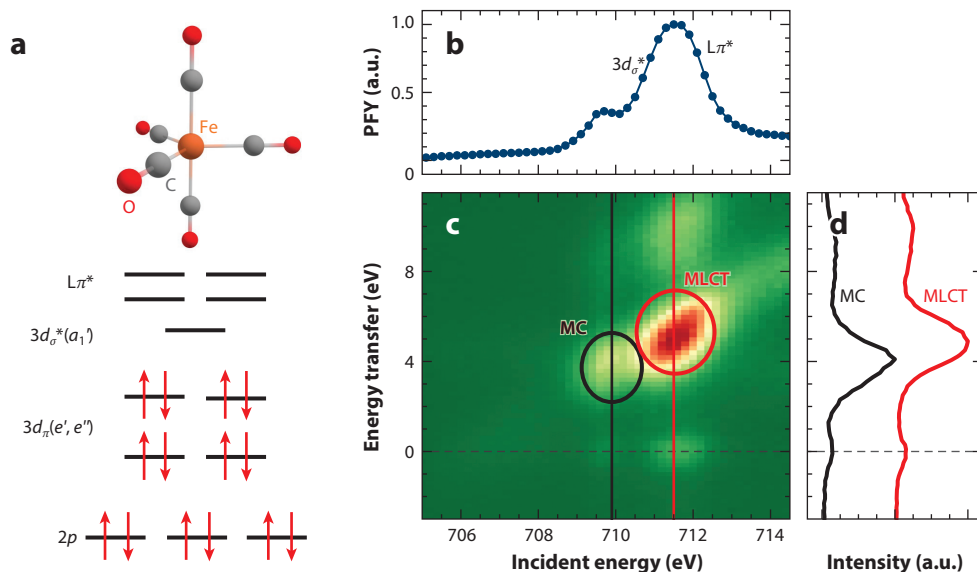


Figure 5

(a) Molecular structure and orbital energy diagram of Fe(CO)₅. (b) PFY X-ray absorption spectroscopy spectrum and (c) RIXS map of Fe(CO)₅ measured at the Fe L₃-edge. The dominant core-excited intermediate states in the PFY spectrum and valence excited final states in the RIXS are labeled according to the involved molecular orbitals from panel a. (d) RIXS spectra extracted at the marked incident energies in panel b. The line colors of the spectra in d match the concomitant vertical lines in the RIXS map in panel c. Abbreviations: L, ligand; MC, metal centric; MLCT, metal-to-ligand charge transfer; PFY, partial fluorescence yield; RIXS, resonant inelastic X-ray scattering.

ultrafast experimental methods for interrogating chemical reaction dynamics. The dominant method used to study the photochemistry of metal carbonyls has been ultrafast vibrational spectroscopy (79–87). Vibrational spectroscopy has been influential but does not directly interrogate the electronic structure. Consequently, the dominant time-resolved method for investigating the reaction dynamics does not characterize the electronic structure during CO ligand dissociation or that of the catalytically active undercoordinated metal complex generated by photodissociation.

Ultrafast electronic spectroscopy in the visible and near-UV spectrum has provided limited insight; specifically, the dominant absorption in this spectral range is associated with MLCT excited states, but the variations in this range have proven difficult to correlate with the variations in photocatalytic reactivity (88). The catalytic properties of undercoordinated organometallic complexes have been shown to vary with both the period and the row of the transition-metal block of elements (89), but a clear explanation for these distinctions and how they relate to changes in electronic structure remains elusive. This makes the photophysics and photochemistry of metal carbonyls a clear case for developing and demonstrating the power of ultrafast 3d L-edge RIXS to understand the nonequilibrium electronic structure of organometallic complexes after initial electronic excitation and in undercoordinated geometries after dissociation and how these properties relate to catalysis.

We have focused on Fe(CO)₅ as an archetypical metal–carbonyl complex. Fe(CO)₅ has a trigonal bipyramidal D_{3h} geometry and a closed-shell, singlet electronic ground state (**Figure 5a**). The optical absorption cross section starts in the near-UV spectrum and is dominated by transitions of predominantly MLCT character (90, 91). These MLCT excited states have a dissociative

character and excitation, with 4.66 eV photons in ethanol solution leading to dissociation of one CO and the creation of an $\text{Fe}(\text{CO})_4$ photofragment with near-unity quantum yield. In solution, the rapid vibrational energy transfer to the solvent suppresses further dissociation. In alcohol solutions, the undercoordinated $\text{Fe}(\text{CO})_4$ photoproduct can form complexes with the solvent. This reactivity arises from the fact that $\text{Fe}(\text{CO})_4$ nominally has an electron deficiency at the Fe center; the 16 valence electrons of Fe in $\text{Fe}(\text{CO})_4$ do not fulfill the 18-electron rule. Furthermore, the Fe center is sterically free to interact with the solvent, making it a strong electrophile. Interestingly, the reactivity of the Fe center also depends on the spin state. When in the lowest-energy closed-shell singlet electronic state, $\text{Fe}(\text{CO})_4$ can form complexes with a variety of saturated alkanes and alcohols, whereas the lowest-energy triplet state proves inert. Prior studies, largely using ultrafast vibrational spectroscopy, investigated the interplay between the $\text{Fe}(\text{CO})_4$ spin state and solute–solvent complexation and the initial branching between the singlet and triplet manifolds of states (79–81). How these initial conditions dictate the resultant catalytic outcomes of the Fe–CO photodissociation remained largely undetermined, and so set the stage for our studies (32–34).

Figure 5b shows the electronic ground-state Fe L-edge absorption spectrum of $\text{Fe}(\text{CO})_5$ dissolved in ethanol. As presented schematically in **Figure 2**, the spectrum in **Figure 5b** clearly shows both metal-centered $\text{Fe } 2p \rightarrow 3d_\sigma^*$ and charge-transfer $\text{Fe } 2p \rightarrow L\pi^*$ transitions. The absorption resonance at 709.5 eV corresponds to population of the unoccupied $3d_\sigma^*$ (a_1') orbital aligned parallel to the axial CO ligands of predominantly $3d$ character. With the incident energy tuned to this resonance, the RIXS spectrum in **Figure 5d** shows final states that correspond to MC-excited states at energy transfers of 4 eV due to $3d_\pi \rightarrow 3d_\sigma^*$ transitions ($\text{Fe } 2p \rightarrow 3d_\sigma^*$ followed by $3d_\pi \rightarrow 2p$). The dominant absorption resonance at 711.5 eV corresponds to $\text{Fe } 2p$ transitions to CO ligand π^* orbitals of e' and e'' symmetry ($\text{Fe } 2p \rightarrow L\pi^*$). The dominance of ligand-character orbitals in a $3d$ metal L-edge absorption spectrum is highly unusual and a consequence of the large metal–ligand orbital hybridization in $\text{Fe}(\text{CO})_5$. The inelastic scattering of X-rays off the 711.5 eV resonance leads to predominantly MLCT excitations $3d_\pi \rightarrow L\pi^*$, as shown in **Figure 5d**. These general characteristics of the Fe L-edge RIXS spectrum of $\text{Fe}(\text{CO})_5$ inform our understanding of the time-resolved RIXS spectra presented in **Figure 6**.

Figure 6a and **b** shows the excited-state RIXS maps collected for two distinct time-delay ranges. The majority of important dynamics have been observed with the incident energy range from 706 to 710 eV and corresponds to $\text{Fe } 2p$ transitions into unoccupied $3d_\sigma^*$ orbitals of predominantly Fe character, with energy transfers in the corresponding RIXS spectra ranging from –2 to 4 eV. The ~300-fs time resolution of the measurement did not allow the CO photodissociation to be followed directly, but the measurement does enable the $\text{Fe}(\text{CO})_4$ electronic state populations formed directly by photodissociation to be characterized. The changes in the RIXS spectrum associated with the formation of the $\text{Fe}(\text{CO})_4$ photofragment reflect multiple potential effects. The unoccupied $3d_\sigma^*$ orbital for closed-shell electronic configurations transforms as the totally symmetric irreducible representation for both $\text{Fe}(\text{CO})_5$ in D_{3h} symmetry and $\text{Fe}(\text{CO})_4$ in the expected C_{2v} symmetry. However, the reduction in ligand field strength resulting from the loss of a CO ligand shifts this unoccupied orbital to lower energy (see **Figure 6c**). This and the exchange interaction stabilize open-shell triplet configurations (see **Figure 6g**). Prior studies have demonstrated that the lowest-energy state for gas phase $\text{Fe}(\text{CO})_4$ has a triplet configuration 3B_2 , whereas solvation of the $\text{Fe}(\text{CO})_4$ fragment makes the closed-shell 1A_1 solute–solvent complex the lowest-energy electronic state in solution (79). Ultrafast vibrational spectroscopy studies show clear evidence for both 3B_2 and 1A_1 complexes in solution after delays of roughly 10 ps (81). How the photodissociation process influences the initial population of singlet and triplet states, however, cannot be determined with vibrational spectroscopy because the variation in the carbonyl stretching spectrum induced by a change between singlet and triplet configurations is less

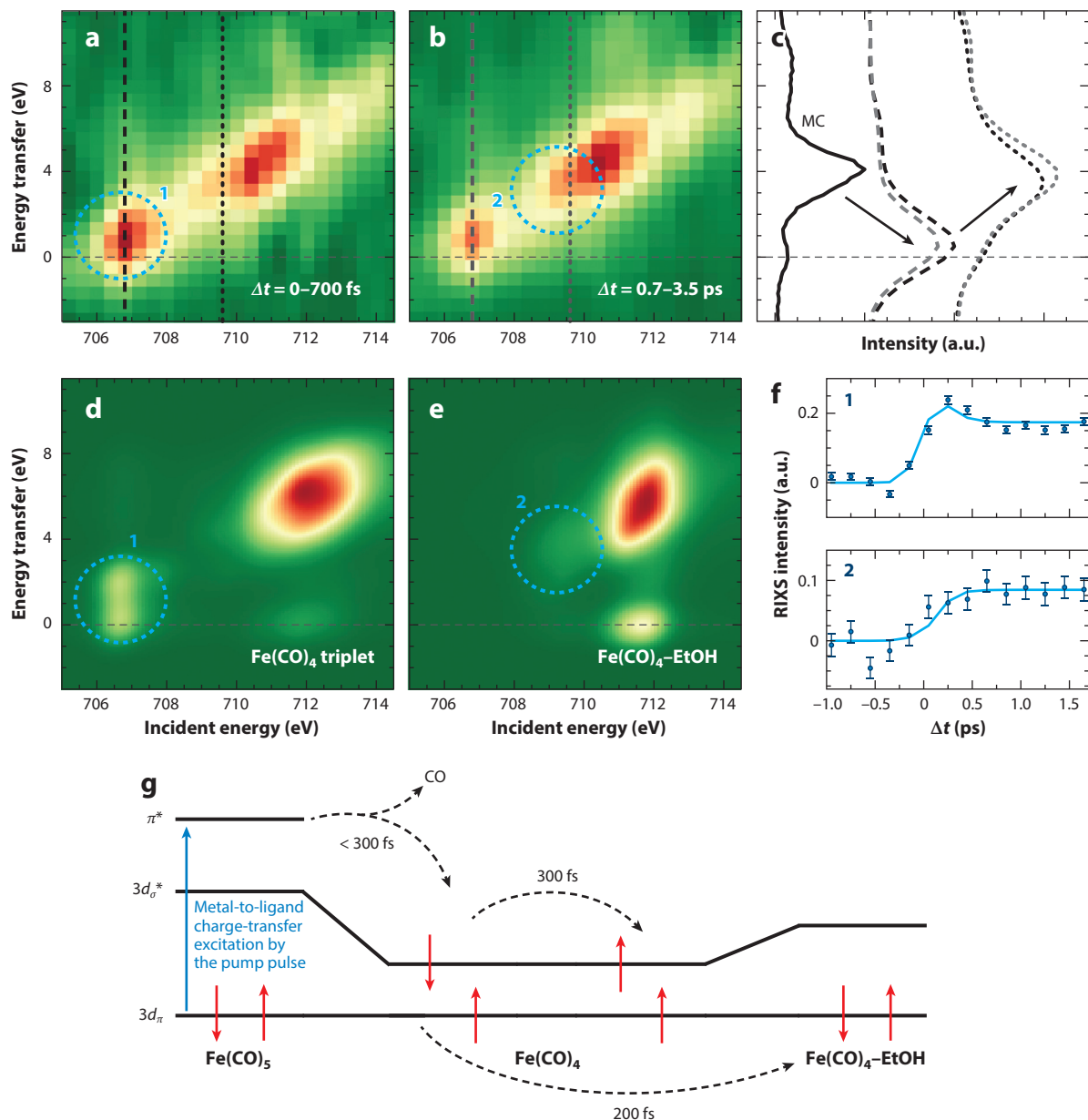


Figure 6

Measured resonant inelastic X-ray scattering (RIXS) maps recorded at (a) early and (b) late time delays during the ligand-exchange dynamics of Fe(CO)_5 . (c) RIXS spectra extracted at the marked incident energies in panels a and b compared to the analog RIXS spectrum of the ground state from Figure 5d, revealing a significant decrease in energy transfer for the metal-centric (MC) ($3d_\pi \rightarrow 3d_\sigma^*$) transitions. The changes in intensity at different delays show the time-dependent population of the different transient species. (d) Calculated RIXS map of the Fe(CO)_4 triplet and (e) the EtOH-bound Fe(CO)_4 singlet, whose spectral signatures dominate the experimental spectra. (f) Delay traces acquired by following the integrated intensity in regions 1 and 2 of the experimental RIXS maps as a function of pump-probe time delay. (g) Schematic molecular orbital energy diagram representing the ligand-exchange dynamics in Fe(CO)_5 with ultrafast loss of a CO and subsequent branching between the triplet Fe(CO)_4 and the EtOH-bound Fe(CO)_4 singlet (blue arrow represents the metal-to-ligand charge-transfer excitation by the pump pulse). Figure adapted with permission from Reference 32; copyright 2015 Nature Research.

than the spectral shifts and broadening caused by the excess internal vibrational energy after the photodissociation reaction. This, as well as how photodissociation and ligand association modulate frontier-orbital interactions, is made accessible with femtosecond time-resolution RIXS.

Determining the initial distribution of $\text{Fe}(\text{CO})_4$ electronic states and characterizing the changes in metal–ligand covalency formed by CO photodissociation are the key findings of our Fe L-edge RIXS studies of $\text{Fe}(\text{CO})_5$. Photodissociation generates a new $\text{Fe } 2p \rightarrow 3d_{\sigma}^*$ X-ray absorption resonance at 706.5 eV, as shown in **Figure 6a** (region 1), that undergoes a partial depletion with a 200–300-fs time constant. Inspection of the RIXS spectrum generated at this resonance also shows ultrafast spectral changes. Specifically, the decay of a weak anti-Stokes Raman signal at negative energy transfer provides a clear signature of the decay of an electronic excited-state time correlated with a rise in the difference signal generated by excitation at 709.5 eV in the energy transfer range from 2 to 4 eV (see **Figure 6f,g**). The assignment and interpretation of these spectral features relies on *ab initio*–calculated RIXS maps for distinct electronic states and nuclear geometries. Two such maps can be found in **Figure 6d,e** that prove critical to interpreting the experimental spectra in **Figure 6a,b**.

The simulated spectra confirmed that the 706.5 eV resonance corresponds to open-shell electron configurations with partial occupations of the $3d_{\pi}$ and $3d_{\sigma}^*$ orbitals. For picosecond time delays, prior experiments indicate that this corresponds to the $^3\text{B}_2$ lowest-energy triplet state, an intuitive interpretation strongly reinforced by the calculated spectrum shown in **Figure 6d**. The weak anti-Stokes Raman signal (33), in the absence of a spin flip during the RIXS process, cannot be assigned to excitation of $\text{Fe}(\text{CO})_4$ complexes in the $^3\text{B}_2$ electronic configuration, as the $^3\text{B}_2$ state is the lowest-energy triplet state. This indicates that the electronic anti-Stokes Raman signal corresponds to the excitation of a quickly decaying electronic excited state. The common energy of the X-ray absorption at 706.5 eV suggests resonant scattering off the same $3d_{\sigma}^*$ unoccupied molecular orbital. This makes the $^1\text{B}_2$ excited state involving the same orbital occupation, but different spin orientation, a viable candidate, an assignment strongly supported by the calculated RIXS spectra (32, 34). This $^1\text{B}_2$ excited state had not been previously observed experimentally, and its detection highlights the power of metal L-edge RIXS spectroscopy to identify and differentiate between distinct MC states. The time correlation between the decay of the $^1\text{B}_2$ excited state and the appearance of an increased intensity at incident energies of around 709.5 eV and energy transfers of from 3 to 4 eV (region 2 in **Figure 6b,e**) supports the assignment of this to the closed-shell $^1\text{A}_1$ lowest-energy singlet state of the $\text{Fe}(\text{CO})_4$ photofragment. Calculated spectra confirmed the $^1\text{A}_1$ electronic state and the close proximity of the solvent to the Fe open coordination site. Decay of the $^1\text{B}_2$ excited state does not result in complete decay of the 706.5 eV resonance. This is consistent with the population of the $^3\text{B}_2$ state, also confirmed by the calculated RIXS fingerprint in **Figure 6d**. Orbital interactions of the undercoordinated Fe center with a solvent molecule partially restores covalent interactions and shifts the $3d_{\sigma}^*$ orbital to higher energies compared to the free fragments. Accordingly, the $\text{Fe } 2p \rightarrow 3d_{\sigma}^*$ absorption resonance and the $3d_{\pi} \rightarrow 3d_{\sigma}^*$ RIXS transitions shift to higher energies (**Figure 6g**).

3. OUTLOOK

Valence RIXS investigations provide a unique perspective on the electronic structure of $3d$ transition-metal complexes. Given the technical challenges associated with soft X-ray RIXS measurements on solution phase samples, a limited number of steady-state experiments have been conducted to date, with even fewer time-resolved investigations of the electronic excited-state structure of transition-metal complexes. The limited number of investigations clearly reflects the technical difficulties associated with the measurements described in Section 2. The breadth of

science that can be addressed with time-resolved RIXS and the potential impact of such investigations, however, provide enthusiasm for the future, because of the recent development of superconducting accelerators for X-ray free-electron laser (XFEL) sources. The reduction in resistive heating in superconducting accelerators enables significant increases in average current and repetition rate. This increase in repetition rate will be transformative for ultrafast soft X-ray RIXS measurements in solution because the related increase in average photon flux (keeping the energy per X-ray pulse constant) directly translates into an increase in the signal-to-noise ratio. The high absorption cross section and femtosecond core-hole lifetime in the soft X-ray energy range exclude using higher X-ray pulse energies because that leads to significantly distorted spectra.

The European XFEL Facility is based on a superconducting accelerator and the first X-ray laser in the soft-to-hard X-ray range to provide repetition rates on the order of tens of kilohertz (92). Utilization of the high repetition rate has been slowed by the burst-mode pulse structure, in which up to 2,700 pulses occur in 0.6 ms followed by 99.4 ms with no pulses. While the densest fill pattern, with a 220-ns gap between X-ray pulses, leaves insufficient time to replace the sample with standard liquid jets and beam spot sizes, kilohertz repetition rates should be feasible and represent an important improvement over normal conducting accelerators with repetition rates of 120 Hz or less. XFELs based on superconducting accelerators, such as the Linac Coherent Light Source II (LCLS-II) currently under construction, can also produce symmetric pulse structures with evenly spaced pulses. LCLS-II will support variable repetition rates up to 1 MHz (93). For repetition rates as high as 100 kHz, pulse energies comparable to those used in the experiments described in this review will be achievable. This presents a clear path to a thousandfold increase in signal compared to the 120 Hz used for the examples discussed above.

The combination of multiple-orders-of-magnitude increases in repetition rate and average photon flux and improvements in the detection efficiency of the RIXS spectrometer will transform the scope of solution phase ultrafast RIXS measurements. The resulting improvements in signal strength will enable the nonequilibrium dynamics of photo-driven chemical transformations to be systematically followed for diverse areas of 3d metal complexes chosen for their chemical interest rather than their experimental feasibility.

These improved ultrafast RIXS and XAS measurements in the soft X-ray energy range present an opportunity to investigate the dynamic interplay between the nuclear and electronic structures. The calculation of molecular potential energy surfaces assumes the electronic structure can be calculated parametrically as a function of nuclear structure. Central to the calculation of the potential energy surfaces that dictate the dynamics of electronic excited states is the presumption that electrons adiabatically respond to changes in nuclear configuration, the Born-Oppenheimer approximation. The foundation of this approximation is the separation of timescales for the motion of electrons and nuclei. This separation breaks down for nuclear configurations with multiple degenerate or near-degenerate electronic states (94–96). The sensitivity of the soft X-ray RIXS measurements to metal–ligand covalency should enable the adiabaticity of the nonequilibrium electronic structure to be accessed experimentally. This capability extends beyond charge-transfer excited states, with recent quantum chemical dynamics simulations of electronic excited-state relaxation in organic molecules also predicting that ultrafast XAS measurements should be able to detect the nonadiabatic transitions between electronic states (97, 98).

More generally, improvements in experimental capabilities should make RIXS characterization of the valence electronic structure of optically generated reactive states and intermediates robust. This will enable systematic studies with sufficient detail to correlate reactivity with electronic structure and potentially identify design principles for controlling nonequilibrium chemical reactivity.

DISCLOSURE STATEMENT

The authors are not aware of any affiliations, memberships, funding, or financial holdings that might be perceived as affecting the objectivity of this review.

ACKNOWLEDGMENTS

We are grateful for the many contributions our collaborators and coworkers have made to the research we review in this article. K.J.G. acknowledges support by the US Department of Energy (DOE), Office of Science, Basic Energy Sciences, Chemical Sciences, Geosciences, and Biosciences Division. K.K. acknowledges support by the US DOE, Office of Science, Basic Energy Sciences (under contract DEAC02-76SF00515). Use of the Linac Coherent Light Source (LCLS), SLAC National Accelerator Laboratory, is supported by the US DOE, Office of Science, Office of Basic Energy Sciences (under contract DE-AC02-76SF00515). Finally, we thank the Helmholtz-Zentrum Berlin für Materialien und Energie for the allocation of synchrotron radiation beamtime.

LITERATURE CITED

1. List B, Lerner RA, Barbas CF. 2000. Proline-catalyzed direct asymmetric aldol reactions. *J. Am. Chem. Soc.* 122:2395–96
2. Knowles WS. 2002. Asymmetric hydrogenations (Nobel lecture). *Angew. Chem. Int. Ed.* 41:1999–2007
3. Noyori R. 2002. Asymmetric catalysis: science and opportunities (Nobel lecture). *Angew. Chem. Int. Ed.* 41:2008–22
4. Sharpless KB. 2002. Searching for new reactivity (Nobel lecture). *Angew. Chem. Int. Ed.* 41:2024–32
5. Chauvin Y. 2006. Olefin metathesis: the early days (Nobel lecture). *Angew. Chem. Int. Ed.* 45:3740–47
6. Grubbs RH. 2006. Olefin-metathesis catalysts for the preparation of molecules and materials (Nobel lecture). *Angew. Chem. Int. Ed.* 45:3760–65
7. Schrock RR. 2006. Multiple metal-carbon bonds for catalytic metathesis reactions (Nobel lecture). *Angew. Chem. Int. Ed.* 45:3748–59
8. MacMillan DWC. 2008. The advent and development of organocatalysis. *Nature* 455:304–8
9. Negishi EI. 2011. Magical power of transition metals: past, present, and future (Nobel lecture). *Angew. Chem. Int. Ed.* 50:6738–64
10. Suzuki A. 2011. Cross-coupling reactions of organoboranes: an easy way to construct C–C bonds (Nobel lecture). *Angew. Chem. Int. Ed.* 50:6722–37
11. Arnold FH. 2019. Innovation by evolution: bringing new chemistry to life (Nobel lecture). *Angew. Chem. Int. Ed.* 58:14420–26
12. Schultz DM, Yoon TP. 2014. Solar synthesis: prospects in visible light photocatalysis. *Science* 343:1239176
13. Skubi KL, Blum TR, Yoon TP. 2016. Dual catalysis strategies in photochemical synthesis. *Chem. Rev.* 116:10035–74
14. Prier CK, Rankic DA, MacMillan DWC. 2013. Visible light photoredox catalysis with transition metal complexes: applications in organic synthesis. *Chem. Rev.* 113:5322–63
15. Karkas MD, Porco JA, Stephenson CRJ. 2016. Photochemical approaches to complex chemotypes: applications in natural product synthesis. *Chem. Rev.* 116:9683–747
16. Arias-Rotondo DM, McCusker JK. 2016. The photophysics of photoredox catalysis: a roadmap for catalyst design. *Chem. Soc. Rev.* 45:5803–20
17. McCusker JK. 2019. Electronic structure in the transition metal block and its implications for light harvesting. *Science* 363:484–88
18. Miller NA, Deb A, Alonso-Mori R, Garabato BD, Glowacki JM, et al. 2017. Polarized XANES monitors femtosecond structural evolution of photoexcited vitamin B-12. *J. Am. Chem. Soc.* 139:1894–99
19. Shelby ML, Lestrangé PJ, Jackson NE, Haldrup K, Mara MW, et al. 2016. Ultrafast excited state relaxation of a metalloporphyrin revealed by femtosecond X-ray absorption spectroscopy. *J. Am. Chem. Soc.* 138:8752–64

20. Mara MW, Hadt RG, Reinhard ME, Kroll T, Lim H, et al. 2017. Metalloprotein entatic control of ligand-metal bonds quantified by ultrafast x-ray spectroscopy. *Science* 356:1276–80
21. Lemke H, Kjær KS, Hartsock RW, van Driel TB, Chollet M, et al. 2017. Coherent structural trapping through wave packet dispersion during photoinduced spin state switching. *Nat. Comm.* 8:15342
22. Cammarata M, Zerdane S, Balducci L, Azzolina G, Mazerat S, et al. 2021. Charge transfer driven by ultrafast spin transition in a CoFe Prussian blue analogue. *Nat. Chem.* 13:10–14
23. Bergmann U, Kern J, Schoenlein RW, Wernet P, Yachandra VK, Yano J. 2021. Using X-ray free-electron lasers for spectroscopy of molecular catalysts and metalloenzymes. *Nat. Rev. Phys.* 3:264–82
24. Ledbetter K, Reinhard ME, Kunnus K, Gallo A, Britz A, et al. 2020. Excited state charge distribution and bond expansion of ferrous complexes observed with femtosecond valence-to-core x-ray emission spectroscopy. *J. Chem. Phys.* 152:074203
25. Gaffney KJ. 2021. Capturing photochemical and photophysical transformations in iron complexes with ultrafast X-ray spectroscopy and scattering. *Chem. Sci.* 12:8010–25
26. Kim KH, Kim JG, Nozawa S, Sato T, Oang KY, et al. 2015. Direct observation of bond formation in solution with femtosecond X-ray scattering. *Nature* 518:385–89
27. van Driel TB, Kjær KS, Hartsock RW, Dohn AO, Harlang T, et al. 2016. Atomistic characterization of the active-site solvation dynamics of a model photocatalyst. *Nat. Comm.* 7:13678
28. Kim JG, Nozawa S, Kim H, Choi EH, Sato T, et al. 2020. Mapping the emergence of molecular vibrations mediating bond formation. *Nature* 582:520–24
29. Vankó G, Bordage A, Glatzel P, Gallo E, Rovezzi M, et al. 2013. Spin-state studies with XES and RIXS: from static to ultrafast. *J. Electron Spectrosc. Relat. Phenom.* 188:166–71
30. Huse N, Kim TK, Jamula L, McCusker JK, de Groot FMF, Schoenlein RW. 2010. Photo-induced spin-state conversion in solvated transition metal complexes probed via time-resolved soft X-ray spectroscopy. *J. Am. Chem. Soc.* 132:6809–16
31. Huse N, Cho H, Hong K, Jamula L, de Groot FMF, et al. 2011. Femtosecond soft X-ray spectroscopy of solvated transition-metal complexes: deciphering the interplay of electronic and structural dynamics. *J. Phys. Chem. Lett.* 2:880–84
32. Wernet P, Kunnus K, Josefsson I, Rajkovic I, Quevedo W, et al. 2015. Orbital-specific mapping of the ligand exchange dynamics of Fe(CO)₅ in solution. *Nature* 520:78–81
33. Kunnus K, Josefsson I, Rajkovic I, Schreck S, Quevedo W, et al. 2016. Anti-Stokes resonant X-ray Raman scattering for atom specific and excited state selective dynamics. *New J. Phys.* 18:103011
34. Kunnus K, Josefsson I, Rajkovic I, Schreck S, Quevedo W, et al. 2016. Identification of the dominant photochemical pathways and mechanistic insights to the ultrafast ligand exchange of Fe(CO)₅ to Fe(CO)₄EtOH. *Struct. Dyn.* 3:043204
35. Jay RM, Norell J, Eckert S, Hantschmann M, Beye M, et al. 2018. Disentangling transient charge density and metal-ligand covalency in photoexcited ferricyanide with femtosecond resonant inelastic soft X-ray scattering. *J. Phys. Chem. Lett.* 9:3538–43
36. Jay RM, Eckert S, Vaz da Cruz V, Fondell M, Mitzner R, Föhlisch A. 2019. Covalency-driven preservation of local charge densities in a metal-to-ligand charge-transfer excited iron photosensitizer. *Angew. Chem. Int. Ed.* 58:10742–46
37. Jay RM, Eckert S, Mitzner R, Fondell M, Föhlisch A. 2020. Quantitative evaluation of transient valence orbital occupations in a 3d transition metal complex as seen from the metal and ligand perspective. *Chem. Phys. Lett.* 754:137681
38. Eckert S, Norell J, Miedema PS, Beye M, Fondell M, et al. 2017. Ultrafast independent N-H and N-C bond deformation investigated with resonant inelastic X-ray scattering. *Angew. Chem. Int. Ed.* 56:6088–92
39. Kjellsson L, Nanda KD, Rubensson JE, Doumy G, Southworth SH, et al. 2020. Resonant inelastic X-ray scattering reveals hidden local transitions of the aqueous OH radical. *Phys. Rev. Lett.* 124:236001
40. Loh ZH, Doumy G, Arnold C, Kjellsson L, Southworth SH, et al. 2020. Observation of the fastest chemical processes in the radiolysis of water. *Science* 367:179–82
41. Cordones AA, Pemmaraju CD, Lee JH, Zegkinoglou I, Ragoussi M-E, et al. 2021. Excited-state charge distribution of a donor- π -acceptor Zn porphyrin probed by N K-edge transient absorption spectroscopy. *J. Phys. Chem. Lett.* 12:1182–88

42. Van Kuiken BE, Cho H, Hong K, Khalil M, Schoenlein RW, et al. 2016. Time-resolved X-ray spectroscopy in the water window: elucidating transient valence charge distributions in an aqueous Fe(II) complex. *J. Phys. Chem. Lett.* 7:465–70
43. Eckert S, Norell J, Jay RM, Fondell M, Mitzner R, et al. 2019. T-1 population as the driver of excited-state proton-transfer in 2-thiopyridone. *Chem. Eur. J.* 25:1733–39
44. Jay RM, Eckert S, Van Kuiken BE, Ochmann M, Hantschmann M, et al. 2021. Following metal-to-ligand charge-transfer dynamics with ligand and spin specificity using femtosecond resonant inelastic X-ray scattering at the nitrogen K-edge. *J. Phys. Chem. Lett.* 12:6676–83
45. Glaser T, Hedman B, Hodgson KO, Solomon EI. 2000. Ligand K-edge X-ray absorption spectroscopy: a direct probe of ligand-metal covalency. *Acc. Chem. Res.* 33:859–68
46. Hocking RK, Wasinger EC, Yan YL, deGroot FMF, Walker FA, et al. 2007. Fe L-edge X-ray absorption spectroscopy of low-spin heme relative to non-heme Fe complexes: delocalization of Fe d-electrons into the porphyrin ligand. *J. Am. Chem. Soc.* 129:113–25
47. de Groot F. 2005. Multiplet effects in X-ray spectroscopy. *Coord. Chem. Rev.* 249:31–63
48. Josefsson I, Kunnus K, Schreck S, Föhlisch A, de Groot F, et al. 2012. Ab initio calculations of X-ray spectra: atomic multiplet and molecular orbital effects in a multiconfigurational SCF approach to the L-edge spectra of transition metal complexes. *J. Phys. Chem. Lett.* 3:3565–70
49. Kunnus K, Josefsson I, Schreck S, Quevedo W, Miedema PS, et al. 2013. From ligand fields to molecular orbitals: probing the local valence electronic structure of Ni²⁺ in aqueous solution with resonant inelastic X-ray scattering. *J. Phys. Chem. B* 117:16512–21
50. Kunnus K, Zhang W, Delcey MG, Pinjari RV, Miedema PS, et al. 2016. Viewing the valence electronic structure of ferric and ferrous hexacyanide in solution from the Fe and cyanide perspectives. *J. Phys. Chem. B* 120:7182–94
51. Lundberg M, Wernet P. 2019. Resonant inelastic X-ray scattering (RIXS) studies in chemistry: present and future. In *Synchrotron Light Sources and Free-Electron Lasers*, ed. E Jaeschke, S Khan, JR Schneider, JB Hastings, pp. 1–52. Cham, Switz.: Springer
52. Siegbahn K. 1982. Electron spectroscopy for atoms, molecules, and condensed matter. *Rev. Mod. Phys.* 54:709–28
53. Kotani A, Shin S. 2001. Resonant inelastic X-ray scattering spectra for electrons in solids. *Rev. Mod. Phys.* 73:203–46
54. Sałek P, Baev A, Gel'mukhanov F, Ågren H. 2003. Dynamical properties of X-ray Raman scattering. *Phys. Chem. Chem. Phys.* 5:1–11
55. Couto RC, Cruz VV, Ertan E, Eckert S, Fondell M, et al. 2017. Selective gating to vibrational modes through resonant X-ray scattering. *Nat. Comm.* 8:14165
56. Vaz da Cruz V, Gel'mukhanov F, Eckert S, Iannuzzi M, Ertan E, et al. 2019. Probing hydrogen bond strength in liquid water by resonant inelastic X-ray scattering. *Nat. Comm.* 10:1013
57. Krause MO, Oliver JH. 1979. Natural widths of atomic K and L levels, K α X-ray lines and several KLL Auger lines. *J. Phys. Chem. Ref. Data* 8:329–38
58. Kunnus K, Rajkovic I, Schreck S, Quevedo W, Eckert S, et al. 2012. A setup for resonant inelastic soft x-ray scattering on liquids at free electron laser light sources. *Rev. Sci. Instrum.* 83:123109
59. Schreck S, Beyé M, Sellberg JA, McQueen T, Laksmono H, et al. 2014. Reabsorption of soft X-ray emission at high X-ray free-electron laser fluences. *Phys. Rev. Lett.* 113:153002
60. Kubin M, Kern J, Gul S, Kroll T, Chatterjee R, et al. 2017. Soft x-ray absorption spectroscopy of metalloproteins and high-valent metal-complexes at room temperature using free-electron lasers. *Struct. Dyn.* 4:054307
61. Gray HB, Beach NA. 1963. Electronic structures of octahedral metal complexes. I. Metal hexacarbonyls and hexacyanides. *J. Am. Chem. Soc.* 85:2922–27
62. Alexander JJ, Gray HB. 1968. Electronic structures of hexacyanometalate complexes. *J. Am. Chem. Soc.* 90:4260–71
63. Jones LH. 1963. Nature of bonding in metal cyanide complexes as related to intensity and frequency of infrared absorption spectra. *Inorg. Chem.* 2:777–80

64. Seidel R, Thurmer S, Moens J, Geerlings P, Blumberger J, Winter B. 2011. Valence photoemission spectra of aqueous $\text{Fe}^{2+/3+}$ and $\text{Fe}(\text{CN})_6^{4-/3-}$ and their interpretation by DFT calculations. *J. Phys. Chem. B* 115:11671–77
65. Lundberg M, Kroll T, DeBeer S, Bergmann U, Wilson SA, et al. 2013. Metal-ligand covalency of iron complexes from high-resolution resonant inelastic X-ray scattering. *J. Am. Chem. Soc.* 135:17121–34
66. Ross M, Andersen A, Fox ZW, Zhang Y, Hong K, et al. 2018. Comprehensive experimental and computational spectroscopic study of hexacyanoferrate complexes in water: from infrared to X-ray wavelengths. *J. Phys. Chem. B* 122:5075–86
67. Hocking RK, Wasinger EC, de Groot FMF, Hodgson KO, Hedman B, Solomon EI. 2006. Fe L-edge XAS studies of $\text{K}_4\text{Fe}(\text{CN})_6$ and $\text{K}_3\text{Fe}(\text{CN})_6$: a direct probe of back-bonding. *J. Am. Chem. Soc.* 128:10442–51
68. Pinjari RV, Delcey MG, Guo M, Odelius M, Lundberg M. 2014. Restricted active space calculations of L-edge X-ray absorption spectra: from molecular orbitals to multiplet states. *J. Chem. Phys.* 141:124116
69. Jay RM, Vaz da Cruz V, Eckert S, Fondell M, Mitzner R, Föhlisch A. 2020. Probing solute-solvent interactions of transition metal complexes using L-edge absorption spectroscopy. *J. Phys. Chem. B* 124:5636–45
70. Jay RM, Eckert S, Fondell M, Miedema PS, Norell J, et al. 2018. The nature of frontier orbitals under systematic ligand exchange in (pseudo-)octahedral Fe(II) complexes. *Phys. Chem. Chem. Phys.* 20:27745–51
71. Norell J, Jay RM, Hantschmann M, Eckert S, Guo M, et al. 2018. Fingerprints of electronic, spin and structural dynamics from resonant inelastic soft X-ray scattering in transient photo-chemical species. *Phys. Chem. Chem. Phys.* 20:7243–53
72. Norman P, Dreuw A. 2018. Simulating X-ray spectroscopies and calculating core-excited states of molecules. *Chem. Rev.* 118:7208–48
73. Engel N, Bokarev SI, Moguilevski A, Raheem AA, Al-Obaidi R, et al. 2017. Light-induced relaxation dynamics of the ferricyanide ion revisited by ultrafast XUV photoelectron spectroscopy. *Phys. Chem. Chem. Phys.* 19:14248–55
74. Ojeda J, Arrell CA, Longetti L, Chergui M, Helbing J. 2017. Charge-transfer and impulsive electronic-to-vibrational energy conversion in ferricyanide: ultrafast photoelectron and transient infrared studies. *Phys. Chem. Chem. Phys.* 19:17052–62
75. Zhang W, Ji M, Sun Z, Gaffney KJ. 2012. Dynamics of solvent-mediated electron localization in electronically excited hexacyanoferrate(III). *J. Am. Chem. Soc.* 134:2581–88
76. Andersson K, Malmqvist PA, Roos BO. 1992. Second-order perturbation theory with a complete active space self-consistent field reference function. *J. Chem. Phys.* 96:1218–26
77. Roos BO, Taylor PR, Siegbahn PEM. 1980. A complete active space SCF method (CASSCF) using a density-matrix formulated super-CI approach. *Chem. Phys.* 48:157–73
78. Godehusen K, Richter T, Zimmermann P, Wernet P. 2017. Iron L-edge absorption spectroscopy of iron pentacarbonyl and ferrocene in the gas phase. *J. Phys. Chem. A* 121:66–72
79. Besora M, Carreon-Macedo J-L, Cowan AJ, George MW, Harvey JN, et al. 2009. A combined theoretical and experimental study on the role of spin states in the chemistry of $\text{Fe}(\text{CO})_5$ photoproducts. *J. Am. Chem. Soc.* 131:3583–92
80. Portius P, Yang J, Sun X-Z, Grills DC, Matousek P, et al. 2004. Unraveling the photochemistry of $\text{Fe}(\text{CO})_5$ in solution: observation of $\text{Fe}(\text{CO})_3$ and the conversion between $^3\text{Fe}(\text{CO})_4$ and $^1\text{Fe}(\text{CO})_4(\text{solvent})$. *J. Am. Chem. Soc.* 126:10713–20
81. Snee PT, Payne CK, Mebane SD, Kotz KT, Harris CB. 2001. Dynamics of photosubstitution reactions of $\text{Fe}(\text{CO})_5$: an ultrafast infrared study of high spin reactivity. *J. Am. Chem. Soc.* 123:6909–15
82. Lim M, Jackson TA, Anfinrud PA. 1995. Binding of Co to myoglobin from a heme pocket docking site to form nearly linear Fe-C-O. *Science* 269:962–66
83. Lim M, Jackson TA, Anfinrud PA. 1997. Ultrafast rotation and trapping of carbon monoxide dissociated from myoglobin. *Nat. Struct. Biol.* 4:209–14
84. Moore JN, Hansen PA, Hochstrasser RM. 1989. Picosecond infrared probing of metal-carbonyl photodissociation products. *J. Am. Chem. Soc.* 111:4563–66
85. Sun X-Z, Grills DC, Nikiforov SM, Poliakov M, George MW. 1997. Remarkable stability of $(\eta^5\text{-C}_5\text{H}_5)\text{Re}(\text{CO})_2\text{L}$ ($\text{L} = n\text{-heptane, Xe, and Kr}$): a time-resolved infrared spectroscopic study of $(\eta^5\text{-C}_5\text{H}_5)\text{Re}(\text{CO})_3$ in conventional and supercritical fluid solution. *J. Am. Chem. Soc.* 119:7521–25

86. Lomont JP, Nguyen SC, Harris CB. 2014. Ultrafast infrared studies of the role of spin states in organometallic reaction dynamics. *Acc. Chem. Res.* 47:1634–42
87. Yang H, Kotz KT, Asplund MC, Wilkens MJ, Harris CB. 1999. Ultrafast infrared studies of bond activation in organometallic complexes. *Acc. Chem. Res.* 32:551–60
88. Joly AG, Nelson KA. 1991. Metal-carbonyl photochemistry in organic solvents: femtosecond transient absorption and preliminary resonance Raman spectroscopy. *Chem. Phys.* 152:69–82
89. Wrighton M. 1974. Photochemistry of metal carbonyls. *Chem. Rev.* 74:401–30
90. Kotzian M, Rosch N, Schroder H, Zerner MC. 1989. Optical spectra of transition-metal carbonyls: Cr(CO)₆, Fe(CO)₅, and Ni(CO)₄. *J. Am. Chem. Soc.* 111:7687–96
91. Rubner O, Engel V, Hachey MR, Daniel C. 1999. A CASSCF/MR-CCI study of the excited states of Fe(CO)₅. *Chem. Phys. Lett.* 302:489–94
92. Altarelli M. 2011. The European X-ray free-electron laser facility in Hamburg. *Nucl. Instrum. Methods Phys. Res. B* 269:2845–49
93. Galayda JN. 2018. The LCLS-II: a high power upgrade to the LCLS. In *Proceedings of the 9th International Particle Accelerator Conference, Vancouver, BC, Canada*, pp. 18–23. Vancouver, Can.: JaCoW Publ.
94. Domcke W, Yarkony DR. 2012. Role of conical intersections in molecular spectroscopy and photoinduced chemical dynamics. *Annu. Rev. Phys. Chem.* 63:325–52
95. Levine BG, Martínez TJ. 2007. Isomerization through conical intersections. *Annu. Rev. Phys. Chem.* 58:613–34
96. Yarkony DR. 1996. Diabolical conical intersections. *Rev. Mod. Phys.* 68:985–1013
97. List NH, Dempwolff AL, Dreuw A, Norman P, Martínez TJ. 2020. Probing competing relaxation pathways in malonaldehyde with transient X-ray absorption spectroscopy. *Chem. Sci.* 11:4180–93
98. Neville SP, Chergui M, Stolow A, Schuurman MS. 2018. Ultrafast X-ray spectroscopy of conical intersections. *Phys. Rev. Lett.* 120:243001